Archived at the Flinders Academic Commons:

http://dspace.flinders.edu.au/dspace/

This is the publisher's copyrighted version of this article.

The original can be found at: http://www.agu.org/journals/jc/jc0502/2004JC002554/
2004JC002554.pdf

© 2005 Journal of Geophysical Research

Cascading-driven upwelling in submarine canyons at high latitudes

Jochen Kämpf

School of Chemistry, Physics and Earth Sciences, Flinders University of South Australia, Adelaide, South Australia, Australia

[1]   Numerical simulations and laboratory experiments confirm my initial research hypothesis stating that dense-water cascading down a submarine canyon induces localized upwelling of deeper water onto the shelf. This process, not described before, is associated with internal deformation radii inherent in the cascading process being less the canyon width and geostrophic adjustment of a density front that establishes along the canyon axis. Since submarine canyons are common to continental margins, this paper has identified a key process triggering the renewal of shelf waters at high latitudes.

Citation: Kämpf, J. (2005), Cascading-driven upwelling in submarine canyons at high latitudes, *J. Geophys. Res.*, *110*, C02007, doi:10.1029/2004JC002554.

1.   Introduction

[2]   Dense-water cascading at continental margins of Antarctica is a vehicle of dense bottom water formation and contributes to the driving and maintenance of the global thermohaline circulation. Recent studies indicate that intrusions of Circumpolar Deep Water (CDW) onto the shelf are a major control of the properties of Antarctic Bottom Water (AABW) [e.g., *Seidov and Haupt*, 2002] that is a mixture between high-salinity shelf waters and CDW. CDW is a relatively warm ($\sim$2°C), oxygen-poor and nutrient-rich water mass that, because of the tilt of density surfaces in the Antarctic Circumpolar Current, occurs below the depth of the shelf break at many places around the Antarctic continent. Intrusions of CDW are evident in most Antarctic shelf regions, that is, in the Weddell Sea [*Ou*, 1991; *Alverson and Owens*, 1996; *Holland*, 2001a, 2001b], in the Ross Sea [*Domack et al.*, 1992; *Hofmann et al.*, 1996; *Jacobs et al.*, 1996], and in Prydz Bay [*Yu et al.*, 1996]. CDW intrusions are believed to control heat and salt budgets of Antarctic shelf seas in interaction with melt of existing sea ice, new-ice formation [e.g., *Jacobs and Comiso*, 1989], and convective stirring of the water column [*Backhaus et al.*, 1997; *Kämpf and Backhaus*, 1998, 1999]. Moreover, CDW intrusions are believed to significantly modify carbon and oxygen exchange rates and to greatly enhance biologic productivity [*Sweeney et al.*, 2000]. Most previous studies suggested that CDW intrusions were topographically steered, but dynamical origins of this upwelling process remained unknown.

[3]   Topographic steering on length scales $\sim$5–10 km is important in the cascading process owing to relatively small internal deformation radii (approximately a few kilometers) inherent in this process [e.g., *Baines and Condie*, 1998]. The internal deformation radius measures the lateral distance over which a density front adjusts to a geostrophic equilibrium [e.g., *Cushman-Roisin*, 1994]. The continental

margin of Antarctica is replete with topographic features of spatial scales exceeding the internal deformation radius. This includes submarine sills, trenches, deep passages, seamounts, and submarine canyons. This paper focuses on submarine canyons ($\sim$5–50 km wide, 50–500 m deep), particularly on those that cut through the shelf break to "connect" a shelf sea with intermediate waters on the continental slope. Laboratory experiments [*Baines and Condie*, 1998] and numerical simulations [e.g., *Chapman and Gawarkiewicz*, 1995; *Kämpf*, 2000] demonstrate the efficient downward geostrophic steering that submarine canyons impose on dense water flow.

[4]   A detailed understanding of the dynamical nature of canyon-flow interactions at high latitudes is essential for a variety of reasons. This includes a better understanding of (1) heat, salt, carbon, and nutrient budgets of Antarctic (and likewise arctic) shelf seas, and (2) factors that modify the driving of the thermohaline deep circulation in the ocean. Another ongoing problem is the adequate parameterization of dense water cascading in general ocean circulation models [e.g., *Campin and Goosse*, 1999] which are still far from being able to resolve mesoscale processes.

[5]   The research hypothesis verified in this paper by both numerical modeling and laboratory experimentation is that dense-water flows in submarine canyons are accomplished by localized upwelling of deeper water onto the shelf, which would be an explanation of the observed CDW intrusions into Antarctic shelf seas. Previous numerical modeling studies focused more on the dynamics of descending dense water plumes and employed methods that removed the barotropic mode by using (1) the rigid-lid approximation [e.g., *Chapman and Gawarkiewicz*, 1995], (2) a reduced-gravity plume model with an ambient ocean being at rest [e.g., *Jungclaus et al.*, 1995], or (3) a bottom-boundary-layer model being decoupled from the ocean above [*Kämpf*, 2000]. As an improvement to previous numerical model applications, this paper employs a barotropic-baroclinic model that couples the three-dimensional, nonhydrodynamic High-Resolution Bottom-Boundary Layer model (HiReBBL), developed and described by *Kämpf* [2000]

and *Kämpf and Fohrmann* [2000], with a barotropic shallow-water-equation model. Laboratory experiments are conducted in addition to this to underpin the numerical findings.

2. Methods

2.1. Description of the Numerical Model

[6] A two-dimensional shallow-water-equation model is employed to capture the barotropic mode inherent with dense-water cascading. Horizontal momentum equations of this model are given by

$$\frac{\partial U}{\partial t} + U\frac{\partial U}{\partial x} + V\frac{\partial U}{\partial y} - fV = -g\frac{\partial \eta}{\partial x} \tag{1a}$$

$$\frac{\partial V}{\partial t} + U\frac{\partial V}{\partial x} + V\frac{\partial V}{\partial y} + fU = -g\frac{\partial \eta}{\partial y}, \tag{1b}$$

where (x, y) are Cartesian horizontal coordinates, t is time, (U, V) is horizontal velocity, $f = -1.4 \times 10^{-4}\ \mathrm{s}^{-1}$ is the Coriolis parameter (considering Antarctic shelves), $g = 9.81\ \mathrm{m\ s}^{-2}$ is acceleration due to gravity, and η is the sea-surface elevation. The vertically integrated form of the continuity equation is given by

$$\frac{\partial \eta}{\partial t} + \frac{\partial}{\partial x}[(H - h^*)U] + \frac{\partial}{\partial y}[(H - h^*)V] + \frac{\partial}{\partial x}(h^*\langle u\rangle)$$
$$+ \frac{\partial}{\partial y}(h^*\langle v\rangle) = 0, \tag{2}$$

where $H(t, x, y) = H_o(x, y) + \eta(t, x, y)$ is the total water depth with H_o being the undisturbed depth and h^* is the constant vertical extension of a bottom-following layer modeled by HiReBBL (see below) with vertically averaged horizontal flow components $\langle u\rangle$ and $\langle v\rangle$. According to (1) and (2), barotropic flow is initiated by means of a lateral transport divergence in the BBL.

[7] HiReBBL consists of a bottom-following ocean layer of constant thickness h^* that is resolved by constant vertical grid spacing. The governing equations are cast in a rotated, bottom-following coordinate system, being similar to sigma coordinates [see *Kämpf*, 2000]. An important difference between HiReBBL and sigma-coordinate models is that the vertical coordinate is not being stretched when moving into greater total water depths. This allows for tracing of thin, bottom-arrested gravity currents over highly variable bottom topography without a loss in vertical resolution. Horizontal coordinates (x, y) are Cartesian ones, and a bottom-following vertical coordinate z^* is introduced by

$$z^* = z + H_o - h^*, \tag{3}$$

where z is the conventional vertical Cartesian coordinate and $H_o(x, y)$ is the undisturbed total water depth (sea level variations can be ignored here). Thus the model subdomain employed for HiReBBL ranges from $z^* = -h^*$ at the seafloor to $z^* = 0$ at its surface. Note that h must be chosen large enough so that BBL dynamics do not interfere with vertical boundary conditions at $z^* = 0$. After conversion to z^* coordinates, conservation equations for momentum and

volume in the bottom-following subdomain can be written as [*Kämpf*, 2000]

$$\frac{\partial u}{\partial t} + Adv(u) - fv = -\frac{1}{\rho_o}\frac{\partial P}{\partial x} + \frac{\partial H_o}{\partial x}g' + Diff(u), \tag{4a}$$

$$\frac{\partial v}{\partial t} + Adv(v) + fu = -\frac{1}{\rho_o}\frac{\partial P}{\partial y} + \frac{\partial H_o}{\partial y}g' + Diff(v), \tag{4b}$$

$$\frac{\partial w^*}{\partial t} + Adv(w^*) = -\frac{1}{\rho_o}\frac{\partial P}{\partial z^*} - \gamma g' + Diff(w^*), \tag{4c}$$

$$\frac{\partial u}{\partial x} + \frac{\partial v}{\partial y} + \frac{\partial w^*}{\partial z^*} = 0, \tag{4d}$$

where $Adv(.)$ and $Diff(.)$ denote advection and diffusion operators, P is dynamic pressure, $\rho_o = 1028\ \mathrm{kg\ m}^{-3}$ is reference density, $g' = \Delta\rho/\rho_o\ g$ is reduced gravity with $\Delta\rho$ being a density anomaly, w^* is vertical velocity, and $\gamma^2 = 1 - (\partial H_o/\partial x)^2 - (\partial H_o/\partial y)^2$. Notice that the use of bottom-following coordinates splits the lateral pressure-gradient force into two parts: a pressure-gradient force parallel to the seafloor and "buoyant-slope" terms that describe acceleration of a dense fluid on a sloping seafloor. *Kämpf* [2000] and *Kämpf and Fohrmann* [2000] give details on turbulence closures employed for lateral and vertical turbulence. Flow of information from the barotropic model to HiReBBL is realized by dynamic boundary conditions in terms of continuity in dynamic pressure; that is, $P = \rho_o g\eta$ at $z^* = 0$. Moreover, horizontal viscous stresses are assumed to vanish at $z^* = 0$, which implies that horizontal flow is depth-independent across the $z^* = 0$ interface. Note that the pressure condition implies that HiReBBL fully simulates barotropic and baroclinic modes. Density variations are predicted from an advection-diffusion equation for salinity (taking temperature to be uniform) and a linear equation of state using a saline contraction coefficient of a value of $\beta = 8 \times 10^{-4}\ \mathrm{psu}^{-1}$. *Kämpf* [2000] and *Kämpf and Fohrmann* [2000] describe the numerical solver of (4a)–(4d). The barotropic model uses an explicit Eulerian-forward time stepping algorithm and an upstream advection scheme.

2.2. Design of Numerical Experiments

[8] A series of numerical experiments has been conducted considering variations in bottom topography, forcing conditions, and parameter settings. Here a selected experiment thereof is discussed being representative of all experiments conducted. Figure 1 displays the idealized bottom topography used. The y axis is aligned parallel to the shelf break, and the x axis points toward the deep ocean. The shape of the ambient continental slope has been constructed by means of a tangens hyperbolicus function. The shelf depth is chosen at 300 m, and the deep ocean is limited to a depth of 1000 m (to reduce computation times). Embedded in this continental margin is a submarine canyon of cosine cross-shape of a width of 50 km. Its amplitude (canyon depth) attains a maximum of ~250 m near the shelf break, but vanishes both
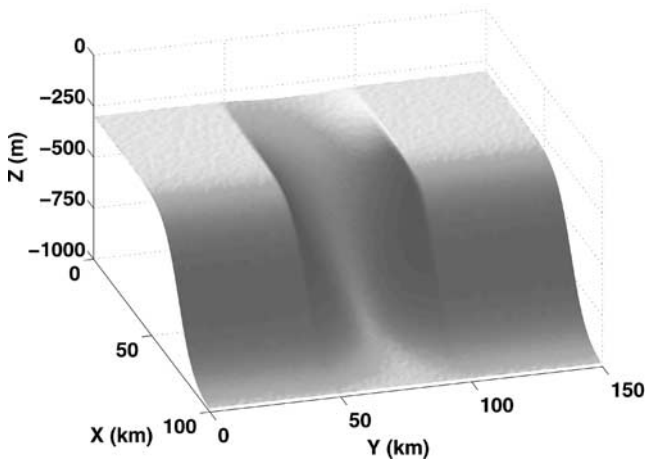
Figure 1. Numerical experiment. Idealized bottom topography.

on the shelf and in the deep ocean. Figure 2a displays contour lines of this topography. Topographic steering of dense-water flows is associated with the buoyant-slope terms in (4a) and (4b). Thus it is very likely that resultant geostrophic near-bottom flows run along contours of bottom slope rather than following topographic contours. This is the motivation to introduce a scalar field, termed "geostrophic slope," by means of

$$\alpha^* = 1000\sqrt{\left(\partial H_o / \partial x\right)^2 + \left(\partial H_o / \partial y\right)^2}, \tag{5}$$

where the initial bottom topography is to be smoothed on spatial scales less the internal deformation radius. Relation (5) gives magnitudes of bottom slope (in units of m/km) on a length scale that is "felt" by baroclinic geostrophic near-bottom flow. Figure 2b displays geostrophic slope contours that are similar but not identical to topographic contours (compare with Figure 2a). Note that maximum geostrophic slopes (>25 m/km) "connect" the canyon with the ambient continental slope in a depth range of 500–700 m. It is therefore likely that canyon plumes follow these geostrophic slope contours and eventually escape from the canyon in this depth range.

[9] Initially, the ocean is at rest and its salinity and temperature fields are spatially uniform. Model forcing is via the prescription of a bottom layer of saline shelf water, 100 m thick, that covers the first 5 km of the shelf over its entire length. To avoid initial numerical noise, the salinity amplitude of this forcing is gradually adjusted from nil to a maximum of 0.5 psu over a period of 5 days. The internal deformation radius associated with this saline bottom layer is ~4 km. Lateral boundaries cutting across the continental slope are cyclically connected. Zero-gradient conditions are employed along shelf and deep-ocean boundaries. Horizontal grid spacings are chosen at 1 km, which is a compromise between (1) resolving the internal deformation radius by a few grid points and (2) covering a reasonably large area. HiReBBL employs 15 layers of a constant vertical grid spacing of 10 m ($h^* = 150$ m). Total simulation time is ~10 days resolved at a time step of 6 s, being limited by the CFL criterion for fast-propagating

gravity waves of the barotropic mode. Time-splitting techniques are not employed.

2.3. Design of Rotation Tank Experiments

[10] Figure 3 shows the laboratory setting. The design of tank experiments has been based on dynamic similarity arguments, summarized in Table 1. A series of tank experiments has been conducted considering variations of tank rotation rate, and forcing and initial conditions within reasonable limits. Here findings of a selected experiment are discussed being representative of all experiments conducted. A glass tank (T), $70 \times 40 \times 40$ cm^3 in dimensions, is rigidly mounted on a rotation platform (R). The rotation rate of the tank has an upper physical limit of $\Omega = 0.3$ cycles per second, corresponding to an inertial period of ~10 s. The rotation sense represents the Southern Hemisphere as in the numerical study. The tank contains a miniature continental margin, made of fiberglass, including a shelf, a shelf break, and a continental slope. The shelf is 10 cm wide. The slope has a bottom inclination of 0.6. Four parallel-aligned submarine canyons (each 5 cm deep and 15 cm wide) are included running perpendicular to the slope. The distance between adjacent channels is ~15 cm. The bottom inclination of channel sidewalls (>1) exceeds that of the ambient slope. The ambient fluid consists of a layer of dense bottom water (salinity is 5 psu) underneath a layer of surface water (freshwater) with a density interface being located below the shelf break. Red dye is added to the lower layer to visualize the proposed upwelling mechanism. To initialize this ambient two-layer stratification, the lower layer is slowly injected near the bottom (using the external reservoir D) while the tank is already at maximum rotation. This technique perfectly suppresses unwanted vertical mixing between the two layers. After this ambient two-layer stratification has been established, saline (salinity is 10 psu) shelf water is slowly and continuously injected at the bottom of the shelf (using the external reservoir S). The density difference between source water with that in the bottom layer is ~5 kg m^{-3}. No dye is added to the dense source water, so that exclusively the traces of dense-water cascading can be seen, not the cascading process in a direct sense. Note that dense shelf water can be anticipated to move away from the source region by means of buoyancy-driven geostrophic longshore flow. A video camera (C) mounted on a frame is used as a monitoring tool. Tank experiments were continued until flow interfered with the tank's downstream face. Typically, this occurred after ~2 min from start, that is, after ~10 inertial periods. Internal deformation radii of the
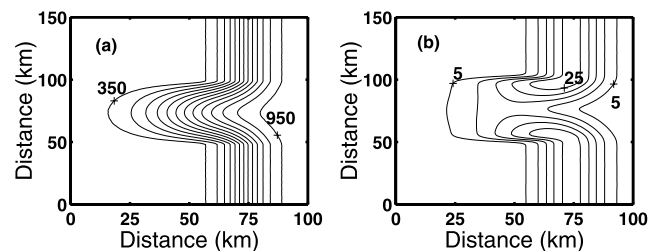

Figure 2. Numerical experiment. Contour lines of (a) topography (CI = 50 m) and (b) geostrophic slope (CI = 5 m/km). See text for details.
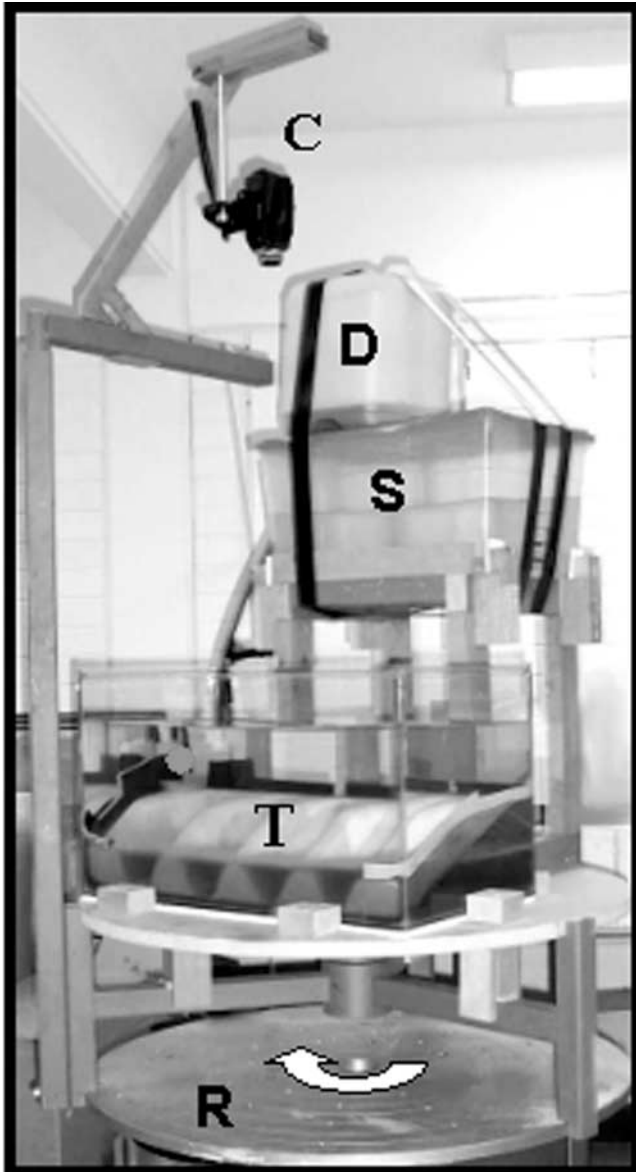
number could be estimated at $Ek = 0.1-0.3$, so that only the lower $10-30\%$ of the canyon plume is influenced by bottom friction, which is similar to $Ek \sim 0.1$ for real flows. On the other hand, the ratio between r and L, that is,

$$\Psi = \frac{\rho}{\Lambda} = \frac{\sqrt{\gamma'\eta}}{\phi\Lambda}, \tag{7}$$

compares the length scale inherent with geostrophic adjustment of a density front with the width of a canyon. If this ratio is small compared with unity, a density front can establish centred along the canyon axis driving geostrophic flow down the canyon. Ratio (7) may be termed "Canyon Rossby Number" as it can be interpreted as a classical Rossby number using the velocity scale of frontal flows on a length scale of the canyon width. This Canyon Rossby Number is ~0.3 in the tank experiments, similar to that of real flows. On the basis of this, the author is confident that baroclinic processes modeled in the rotation tank are dynamically similar to those occurring on polar shelves (and those predicted by this paper's numerical model application).

3. Results and Discussion

[12] Figure 4 displays the evolution of a canyon plume as predicted by the numerical model. The plume is conducted downward along the left side of the canyon. The geostrophic cross-channel balance associated with this flow (see below) explains this asymmetric behavior. Interestingly, the plume escapes from the canyon at a depth of 700 m while following the contours of maximum geostrophic slope. This creates a situation in which, on one side of the canyon, lighter seawater becomes bordered by dense shelf water on one side and dense water being locally injected by the canyon plume (see Figure 4d) on the other side.

[13] Figure 5 shows a snapshot of sea-level anomalies and near-bottom flow vectors at day 5 of the simulation. The canyon plume attains a maximum down-canyon speed of 50 cm s^{-1}. The center of the down-canyon flow corresponds to a tongue of negative sea-level anomalies showing a low-pressure cell (sea-level anomaly is -4 cm) at the entrance of the canyon. Overall, cross-canyon barotropic pressure gradients appear to vanish along the axis of the canyon plume that, accordingly, is mainly a baroclinic feature. Interestingly, a narrow up-canyon flow (speed

Figure 3. Design of the rotation tank experiments. See text for further details. See color version of this figure at back of this issue.

resultant baroclinic flow are much smaller (~4 cm) than the tank dimensions, so that quasi-geostrophic dynamics can establish well before reflection will occur at the downstream face.

[11] Scaling arguments suggest that the internal deformation radius (r), the canyon width (L), the plume thickness (h), and the thickness of the bottom Ekman layer (δ) are the dominant scales associated with canyon-flow interaction. The ratio between the latter two scales gives the Ekman number; that is,

$$Ek = \frac{\delta}{h}, \tag{6}$$

which gives an estimate of the percentage of plume thickness that is controlled by bottom friction. From a series of comparison tank experiments (not shown), the Ekman

Table 1. Scales of Laboratory Flows Compared With Antarctic Flows

| Parameter	Laboratory	Antarctica
Bottom inclination of continental slope	0.6	$0.05-0.2$
Coriolis parameter (f), s^{-1}	~0.5	1.4×10^{-4}
Inertial period ($2\pi/f$)	12.5 s	12.5 h
Thickness of canyon plumes (h)	~1 cm	~50 m
Density anomaly, kg m^{-3}	~5	0.2
Reduced gravity (g') , m s^{-2}	$\sim5 \times 10^{-2}$	$\sim5 \times 10^{-3}$
Plume velocity ($U = (g'h)^{1/2}$), cm s^{-1}	~2	~50
Internal deformation radius ($r = U/f$)	~4 cm	~3.6 km
Canyon width (L)	15 cm	$5-50$ km
Canyon Rossby number (Ro$_C$ = r/L)	~0.3	$0.07-0.7$
Thickness of bottom Ekman layer (δ_e)	$1-3$ mm	~5 m
Ekman number (δ_e/h)	$0.1-0.3$	~0.1
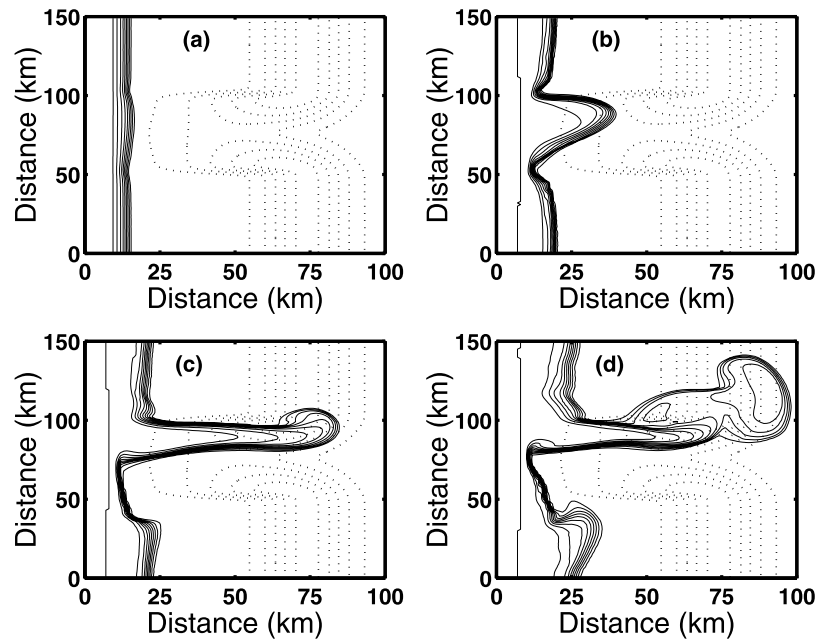
Figure 4. Numerical experiment. Contours of near-bottom salinity anomalies (CI = 0.05 psu) after (a) 1 day, (b) 3 days, (c) 5 days, and (d) 7 days. Geostrophic slope contours (dashed lines) are superimposed.

~30 cm s^{-1}) establishes along the center of the canyon. The forcing of this up-canyon flow must be purely barotropic due to the absence of density anomalies (see Figure 4). Furthermore, this up-canyon flow attains a substantial flow component aligned parallel with sea level contours, pointing to a geostrophic control. In upper parts of the slope, this up-canyon flow merges with an anticyclonic eddy that attains a diameter of ~30 km and a sea level anomaly of ~2.5 cm. Overall, the descending canyon plume is seen to lower the coastal sea level. The barotropic pressure gradient associated with this appears to drive a shelf current that runs opposite to a baroclinic frontal flow that establishes along a density front on the shelf at $x = 15$ km.

[14] Vertical transects reveal the cross-canyon structure of the canyon plume (Figure 6). There is a sharp, almost vertical-aligned density front that intercepts the canyon in its center. The canyon plume attains a thickness of ~100 m. Frictional influences are seen influential in a thin (~10 m) bottom Ekman layer, in agreement with previous studies [*Ezer and Weatherly*, 1990]. The canyon flow comprises a strong baroclinic frontal down-canyon current (speed is ~40 cm s^{-1}) and an adjacent barotropic up-canyon flow (speed is ~−30 cm s^{-1}) centered over the canyon axis. It should be highlighted that the plume's structure and dynamics justifies the model coupling approach requiring baroclinic processes to not interfere with vertical boundary conditions at $z^* = 0$.

[15] The balance of cross-canyon force components provides details of the dynamical nature of the simulated canyon plume. Along-canyon force balances are irrelevant in this, given that the canyon flow is topographically steered and largely geostrophically balanced and that gradients of flow properties do not vary significantly in the down-canyon direction (except in vicinity of the tail and the nose of the plume). Figure 7a displays a cross-canyon section of near-bottom salinity anomalies and the along-canyon flow

component at $x = 40$ km after 5 days of simulation. The regime of (positive) down-canyon flow matches the regime that is occupied by elevated salinities. Up-canyon flow, on the other hand, is a pure barotropic feature existing in the absence of density anomalies. Both down-canyon and up-canyon flows are governed by a cross-canyon geostrophic force balance (Figure 7b). Buoyant-slope effects are the main driver of the down-canyon flow, but bottom-parallel pressure gradients are seen to intensify this flow on one side and to weaken it on the other side of the plume. In contrast to this, sea-level gradients are the sole driver of up-canyon flow. This highlights the importance of the use of a free-surface model in the context of this study.
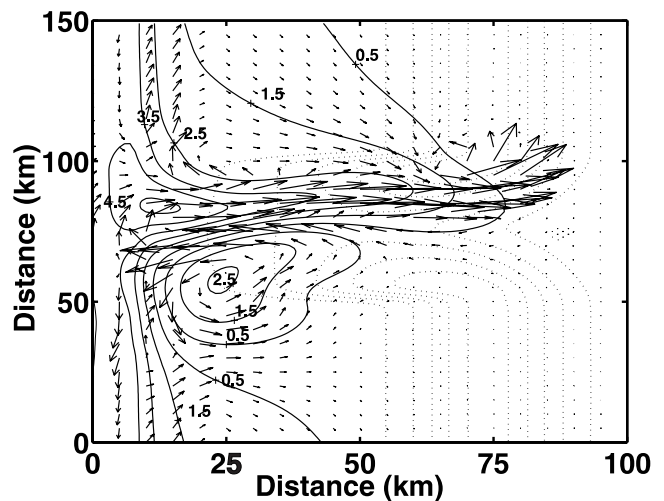

Figure 5. Numerical experiment. Near-bottom velocity field (arrows, maximum speed is 0.5 m/s) and sea-level anomalies (solid lines, CI = 1 cm) after 5 days. Geostrophic slope contours (dashed lines) are superimposed.
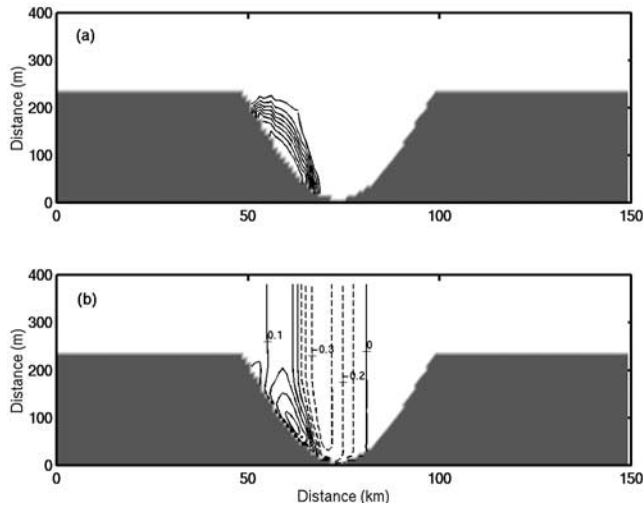
Figure 6. Numerical experiment. Vertical transects across the canyon at x = 40 km after 5 days showing contours of (a) salinity anomalies (CI = 0.05 psu) and (b) down-channel flow speed (CI = 0.1 m/s, dashed lines denote negative values). Model results have been translated to Cartesian coordinates. Note that the view is down the canyon.

[16] The geostrophic balance that establishes in the cross-canyon direction must be associated with geostrophic adjustment of a mesoscale density front that forms along the canyon axis (see Figure 6). This geostrophic adjustment is sketched in Figure 8. According to geostrophic

adjustment theory for a two-layer fluid [e.g., *Cushman-Roisin*, 1994], the resultant speed of the frontal flow scales according to

$$U_1 \approx \sqrt{g'h}. \tag{8}$$

However, geostrophic adjustment does also modify sea-surface elevations. This triggers a barotropic flow in the ambient ocean that runs opposite to the frontal jet. It is trivial to show that the speed of this "return" flow scales according to

$$U_2 = -\frac{h}{H-h}U_1. \tag{9}$$

[17] In the following, the author wishes to verify whether (8) and (9) apply to any cross-canyon section of the simulation canyon plume. To this end, a plume thickness of $h = 100$ m is used (based on analyses of ensembles of vertical salinity profiles along the entire length of the plume), and density anomalies are based on 75% of near-bottom values predicted along the core of the canyon plume (Figure 9a). It is remarkable that this simple approach reproduces the simulated distributions of up-canyon and down-canyon flow speeds at a high accuracy in central parts of the canyon (Figure 9b), which has been confirmed by sensitivity studies considering variations of the salinity forcing. Differences occur on upper portions of the slope, which is governed by an ageostrophic transition of long-shore frontal flow into down-canyon flow (see Figure 5) and near the nose of the plume, where ageostrophic
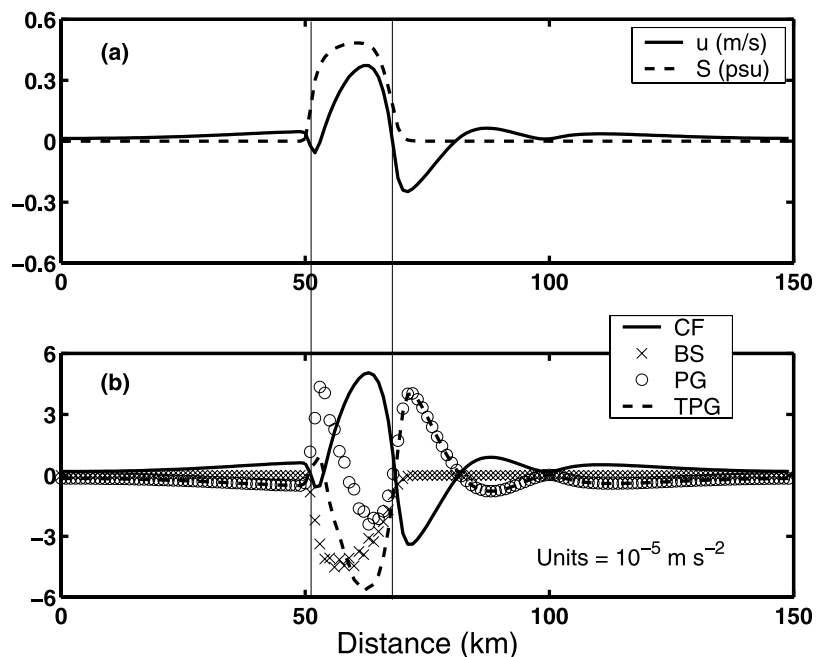

Figure 7. Numerical experiment. Near-bottom distributions across the canyon at x = 40 km after 5 days. (a) Down-canyon flow speed (solid line) and salinity anomalies (dashed line). (b) Force components (per unit mass) in the direction across the canyon. CF: Coriolis force; TPG: total horizontal pressure gradient force; BS: buoyant-slope term; PG: bottom-parallel pressure gradient force including barotropic pressure gradients owing to a sloping sea surface. Vertical lines indicate the margins of the descending dense water plume. Note that the view is down the canyon.
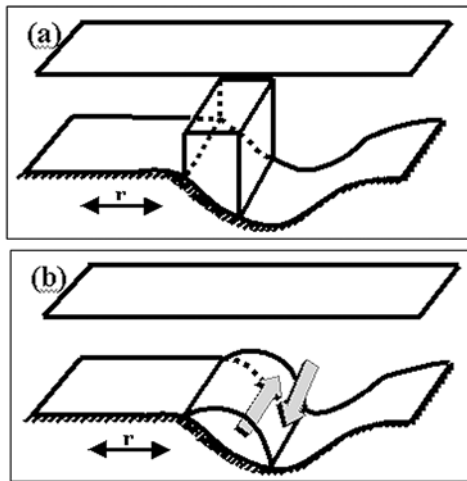
Figure 8. Sketch of geostrophic adjustment (Southern Hemisphere) in a submarine canyon. The internal deformation radius (r) is less the canyon width. (a) Idealized initial conditions of an indefinitely long "wall" of dense water running along the canyon axis. (b) Orientation of resultant frontal flows comprising a baroclinic down-canyon flow and a barotropic up-canyon flow.

effects influence the dynamics. Even though the applicability of a two-layer model to a rather gradually stratified baroclinic flow over irregular topography is somewhat questionable, (9) qualitatively describes the simulated increase in up-canyon flow speed with decreasing water depth. It is worth mentioning that the volume transport of the simulated canyon plume of $\sim$0.5 Sv equals that of the up-canyon flow.

[18] Trajectories of passive Lagrangian tracers, initially released in lower parts of the canyon, reveal the traces of the up-canyon flow (Figure 10a). Since no particle is released on the shelf, the resultant trajectories are exclusively due to barotropic flow and/or entrainment into the canyon plume. It can be seen that the up-canyon flow induces upwelling centered over the canyon axis along the entire length of the canyon. As a result of this, shelf water becomes replaced by deep water in a direct sense. The vehicle of this is a cascading-driven bottom-parallel "overturning" circulation. At later stages of this process, upwelled water parcels become entrained into the canyon plume and thus are carried downward again by the canyon plume (Figure 10b).

[19] Laboratory experiments confirm the existence of both canyon plumes and the associated up-canyon flows (Figure 11), in agreement with the above numerical findings. Up-canyon flows, seen as narrow tongues of red-dyed water, occur within canyons and run opposite to descending canyon plumes that can also be identified. Also indicated are the formations of a cyclonic eddy at the entrance of a canyon and an anticyclonic eddy adjacent to this (compare with Figure 5), as is the entrainment of previously upwelled water into a descending canyon plume (compare with Figure 10). Interestingly, upwelled water tends to move toward the dense shelf water source. This is not seen in trajectories of the numerical model application (see Figure 10), but is in agreement with the

simulated shelf currents (see Figure 6). Differences in the dynamics of adjacent canyon plumes, seen in the laboratory experiment, are most likely due to a close spacing between canyons and close proximity of outer canyons to sidewalls. Nevertheless, the rotation tank experiments appear to capture the key processes of the cascading process.

[20] Mesoscale topographic steering induced by geostrophic adjustment of a density front can be expected to occur for topographic features that have a spatial scale exceeding the internal deformation radius such as submarine sills, trenches, or deep passages. An example of this is flow through the deep Orkney Passage, which is one of the four passages that connect the Weddell Sea with the Scotia Sea. Figure 12 shows LADCP measurements of flow through this passage together with isopycnals [*Naveira Garabato et al.*, 2002]. In the context of this paper, the author merely wishes to point out a striking similarity between observed flow and density patterns with those of the simulated canyon flow (see Figure 6). It is also noteworthy that the "Canyon Rossby Number" associated with baroclinic flow through the Orkney Passage can be estimated at $\psi < 0.1$, being similar to that in numerical and laboratory experiments discussed in this paper.

4. Conclusions

[21] Numerical and laboratory experiments confirm the author's initial research hypothesis stating that dense-water cascading in a submarine canyon at high latitude triggers a localized up-canyon flow (upwelling) of deeper water onto the shelf. Simple theoretical considerations suggest that the magnitude of resultant flows can be estimated by means of a
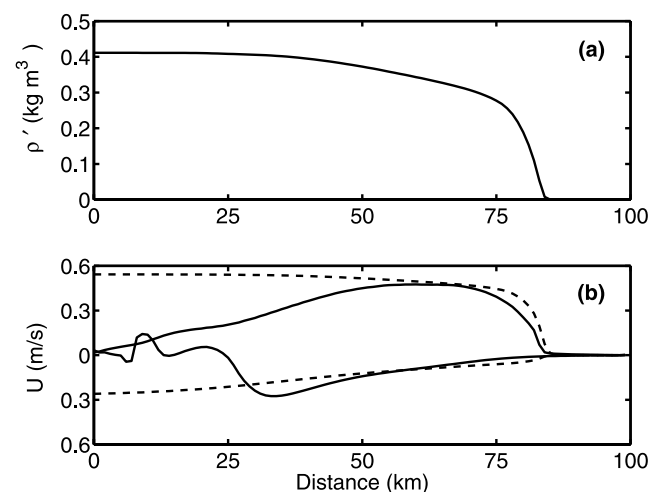

Figure 9. Numerical experiment. Results after 5 days. (a) Distribution of near-bottom density anomalies at y = 90 km along the axis of the descending plume. (b) Distributions of near-bottom flow speed (1) at y = 90 km along the axis of the descending plume (solid line; showing positive values throughout) and (2) at y = 79 km along the axis of adjacent up-canyon flows (solid line; showing mostly negative values). Dashed lines show results from simple geostrophic adjustment considerations (see text).
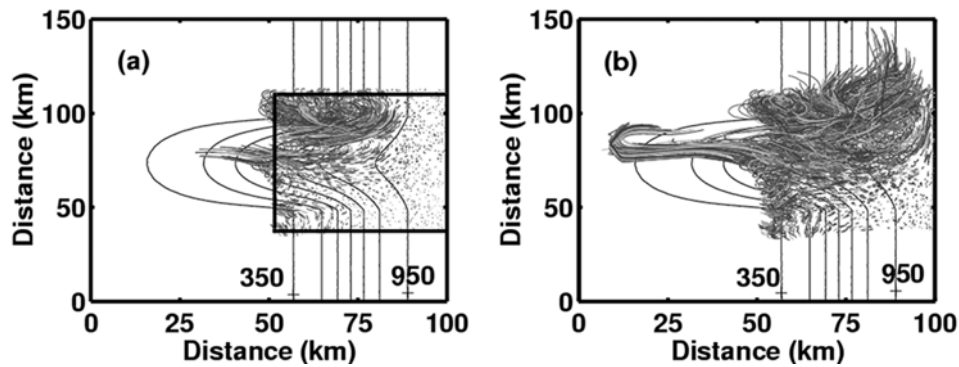
Figure 10. Numerical experiment. Trajectories of 2000 Lagrangian tracers (initially distributed at random within the limits of the rectangle shown in the left frame) (a) from day 0 to day 5 and (b) from day 0 to day 7.5.

two-dimensional geostrophic adjustment of a density front in an assumed two-layer ocean. As a result of this, down-canyon and up-canyon flows attain transports of the same order of magnitude. The proposed upwelling mechanism, not reported before, would give a reasonable explanation of CDW intrusions observed in most antarctic shelf seas. Details of this, however, need to be verified on a case by case basis. Nevertheless, the proposed process is very likely to occur during the period of dense-water formation and spreading (late winter) and presumably is a key control of the budgets of heat, salt, carbon, and nutrients including dissolved metals in antarctic (and likewise arctic) shelf seas.

[22] Numerical experiments, presented above, indicate that baroclinic flows inherent with the cascading process tend to follow geostrophic slope contours rather than topographic contours. The reason for this is the dominance of buoyant-slope terms in the momentum equations in the forcing of these flows. Therefore the use of geostrophic slope contours, if known, may be a cost-efficient tool to predict the injection level of canyon flows.

[23] Much of the margin of Antarctica hosts two features identifiable in hydrographic and/or velocity observations: the Antarctic Slope Front (ASF) and the Antarctic Coastal Current [*Heywood et al.*, 2004]. The ASF defines the boundary between cold, relatively fresh waters filling the Antarctic continental shelf and the warmer, more saline waters farther offshore [e.g., *Jacobs*, 1991] and is associated with a westward geostrophic transport around Antarctica. Associated with this is a fast frontal jet that is strongly constrained to the continental slope at depths varying between 500 and 1500 m [*Heywood et al.*, 2004, and references therein]. On the other hand, the Antarctic Coastal Current is a fast, shallow flow over the continental shelf and is often associated with the front of the ice shelf [e.g., *Jacobs*, 1991]. Interestingly, where the shelf is broad, the coastal current separates from the ASF and travels over the shelf. This separation is very similar to the flow situation shown in Figure 7. The author therefore postulates that it is injections of canyon plumes that maintain the ASF, whereas the Antarctic Coastal Current is likely to be caused by a combination of buoyancy forcing and other processes such as wind-driving upwelling along the ice edge [e.g., *Cushman-Roisin*, 1994]. It should be pointed out that the proposed canyon
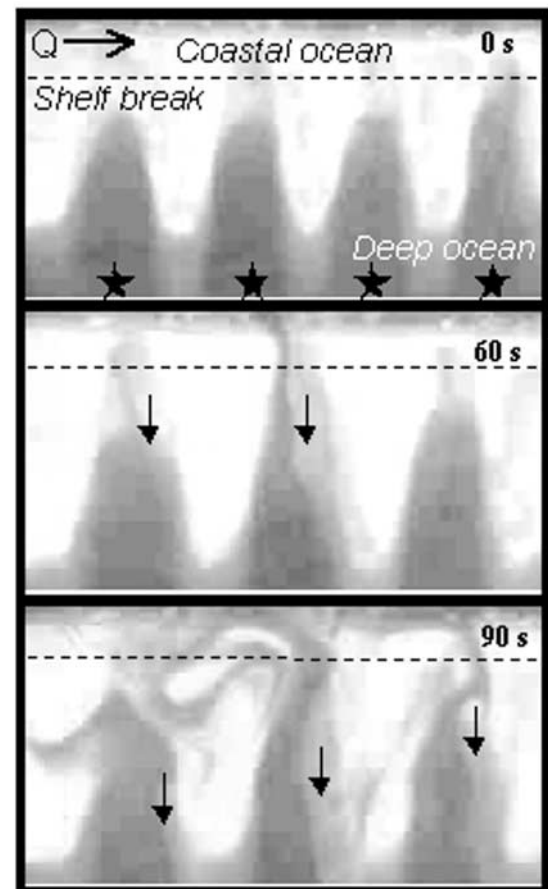

Figure 11. Laboratory experiment. Plane views showing spatial distributions of the interface of the bottom layer (red dye) (top) initially, (middle) after 60 s = 4.4 inertial periods, and (bottom) after 90 s = 6.7 inertial periods. Submarine channels run from top to bottom in each frame. Stars indicate locations of canyon axes. The source (Q) of dense shelf water is located in the upper left corner in each frame. Arrows highlight descending dense-water plumes. See color version of this figure at back of this issue.
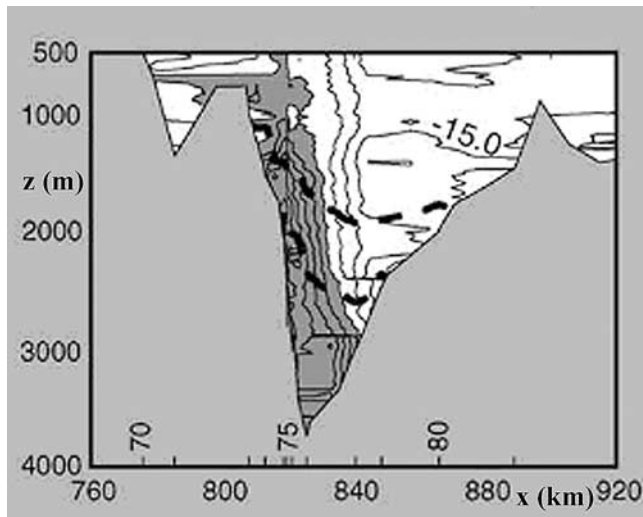
Figure 12. Field measurements. Vertical transect across the deep Orkney Passage showing the cross-track component of LADCP velocity. Dark (white) shades denote northward (southward) flow (CI = 5 cm/s). Dashed lines represent isopycnic water mass boundaries. Station positions are marked on the lower axis (showing distance in kilometers). From *Naveira Garabato et al.* [2002].

flow forms a direct connection between shelf seas and the deep ocean. The parameterization of *Campin and Goosse* [1999], commonly used in large-scale models [e.g., *Doney and Hecht*, 2001] and being based on such a direct connection, is therefore justifiable, although it does not capture the up-canyon return flow.

[24] Recent AnSlope (Cross-slope exchanges at the Antarctic Slope Front) field experiments have established a comprehensive suite of oceanographic data in conjunction with high-resolution bathymetric surveys of the western Ross Sea. Preliminary findings, reported in two cruise reports (A. Gordon, AnSlope Cruise #1 *Nathaniel B. Palmer* 0302, McMurdo, Antarctica to Port Lyttelton, New Zealand; 25 February to 9 April 2003 (available at http://www.ldeo.columbia.edu/res/div/ocp/projects/anslope. shtml) and M. Visbeck, AnSlope Cruise #2 *Nathaniel B. Palmer* 0402; 23 February to 10 April 2004, (available at http://www.ldeo.columbia.edu/res/div/ocp/projects/anslope. shtml)), give many details on topographically steered dense water flows and occasional intrusions of modified CDW onto the shelf. Moreover, AnSlope mooring data show that tidal dynamics, not considered in this paper, strongly modify cross-slope exchanges. Thus, in real situations the predominance of the proposed cascading-upwelling mechanism presumably depends on many factors such as properties of dense water sources, existence of ambient larger-scale circulation pattern, and tidal dynamics, which could not be addressed within the scope (and page limit) of this paper. Nevertheless, theoretical findings reported here might aid in the interpretation of AnSlope data. It should be noted that modified CDW found on the West Antarctic Peninsula Continental Shelf is not related to dense-water production. Instead of this, formation of this water mass can be explained by a simple diffusion model [*Smith et al.*,

1999]. This, however, does not contradict findings reported here.

References

Alverson, K., and W. B. Owens (1996), Topographic preconditioning of open-ocean deep convection, *J. Phys. Oceanogr.*, *26*, 2196–2213.

Backhaus, J. O., H. Fohrmann, J. Kämpf, and A. Rubino (1997), Formation and export of water masses produced in Arctic shelf polynyas, *ICES J. Mar. Sci.*, *54*, 366–382.

Baines, P. G., and S. Condie (1998), Observations and modelling of Antarctic downslope flows: A review, in *Ocean, Ice, and Atmosphere: Interactions at the Antarctic Continental Margin*, *Antarct. Res. Ser.*, vol. 75, edited by S. S. Jacobs and R. F. Weiss, pp. 29–49, AGU, Washington, D. C.

Campin, J.-M., and H. Goosse (1999), Parameterization of density-driven downsloping flow for a coarse-resolution ocean model in z-coordinate, *Tellus, Ser. A*, *51*, 412–430.

Chapman, D. C., and G. Gawarkiewicz (1995), Offshore transport of dense shelf water in the presence of a submarine canyon, *J. Geophys. Res.*, *100*, 13,373–13,387.

Cushman-Roisin, B. (1994), *Introduction to Geophysical Fluid Dynamics*, 320 pp., Prentice-Hall, Upper Saddle River, N. J.

Domack, E. W., E. Schere, C. McClennen, and J. Anderson (1992), Intrusion of circumpolar deep water along the Bellingshausen Sea continental shelf, *Antarct. J. U. S.*, *27*, 71.

Doney, S. C., and M. W. Hecht (2001), Antarctic Bottom Water formation and deep-water chlorofluorocarbon distributions in a global ocean climate model, *J. Phys. Oceanogr.*, *32*, 1642–1666.

Ezer, T., and G. L. Weatherly (1990), A numerical study of the interaction between a deep cold jet and the bottom boundary layer of the ocean, *J. Phys. Oceanogr.*, *20*, 801–816.

Heywood, K. J., A. C. Naveira Garabato, D. P. Stevens, and R. D. Muench (2004), On the fate of the Antarctic Slope Front and the origin of the Weddell Front, *J. Geophys. Res.*, *109*, C06021, doi:10.1029/2003JC002053.

Hofmann, E. E., J. M. Klinck, C. M. Lascara, and D. Smith (1996), Water mass distribution and circulation west of the Antarctic Peninsula and including Bransfield Strait, in *Foundations for Ecological Research West of the Antarctic Peninsula*, *Antarct. Res. Ser.*, vol. 70, edited by R. M. Ross, E. E. Hofmann, and L. B. Quetin, pp. 61–80, AGU, Washington, D. C.

Holland, D. M. (2001a), Transient sea-ice polynya forced by environmental flow variability, *Prog. Oceanogr.*, *48*, 475–532.

Holland, D. M. (2001b), Explaining the Weddell Polynya—A large ocean eddy shed at Maud Rise, *Science*, *292*, 1697–1700.

Jacobs, S. S. (1991), On the nature and significance of the Antarctic Slope Front, *Mar. Chem.*, *35*, 9–24.

Jacobs, S. S., and J. C. Comiso (1989), Sea ice and oceanic processes on the Ross Sea continental shelf, *J. Geophys. Res.*, *94*, 18,195–18,211.

Jacobs, S. S., H. H. Hellmer, and A. Jenkins (1996), Antarctic ice sheet melting in the southeast Pacific, *Geophys. Res. Lett.*, *23*, 957–960.

Jungclaus, J. H., J. O. Backhaus, and H. Fohrmann (1995), Outflow of dense water from the Storfjord in Svalbard: A numerical model study, *J. Geophys. Res.*, *100*, 24,719–24,728.

Kämpf, J. (2000), Impact of multiple submarine channels on the descent of dense water at high latitudes, *J. Geophys. Res.*, *105*, 8753–8773.

Kämpf, J., and J. O. Backhaus (1998), Shallow, brine-driven free convection in polar oceans: Nonhydrostatic numerical process studies, *J. Geophys. Res.*, *103*, 5577–5593.

Kämpf, J., and J. O. Backhaus (1999), Ice-ocean interactions during shallow convection under conditions of steady winds: Three-dimensional numerical studies, *Deep Sea Res., Part II*, *46*, 1335–1355.

Kämpf, J., and H. Fohrmann (2000), Sediment-driven downslope flow in submarine canyons and channels: Three-dimensional numerical experiments, *J. Phys. Oceanogr.*, *30*, 2302–2319.

Naveira Garabato, A. C., E. L. McDonagh, D. P. Stevens, K. Heywood, and R. J. Sanders (2002), On the export of Antarctic Bottom Water from the Weddell Sea, *Deep Sea Res., Part II*, *49*, 4715–4742.

Ou, H. W. (1991), Some effects of a seamount on oceanic flows, *J. Phys. Oceanogr.*, *21*, 1835–1845.

Seidov, D., and B. J. Haupt (2002), On the role of inter-basin surface salinity contrasts in global ocean circulation, *Geophys. Res. Lett.*, *29*(16), 1800, doi:10.1029/2002GL014813.

Smith, D. A., E. E. Hofmann, J. M. Klinck, and C. M. Lascara (1999), Hydrography and circulation of the West Antarctic Peninsula Continental Shelf, *Deep Sea Res., Part I*, *46*, 925–949.

Sweeney, C., W. O. Smith, B. Hales, D. A. Hansell, C. A. Carlson, L. A. Codispoti, L. I. Gordon, F. J. Millero, and T. Takahashi (2000), Nutrient and carbon removal ratios and fluxes in the Ross Sea, Antarctica, *Deep Sea Res., Part II*, *47*, 3395–3422.

Yu, H. H., J. L. Su, and Y. T. Miao (1996), Upwelling of deep water and formation for bottom water near Prydz Bay (in Chinese), in *Studies on the Interaction Between the Antarctica and Global Climatic Environment*, edited by Z. Xiuji and L. Longhua, pp. 140–147, China Meteorol., Beijing.

————————————

J. Kämpf, School of Chemistry, Physics and Earth Sciences, Flinders University of South Australia, GPO Box 2100, Adelaide, SA 5001, Australia. (jochen.kaempf@flinders.edu.au)
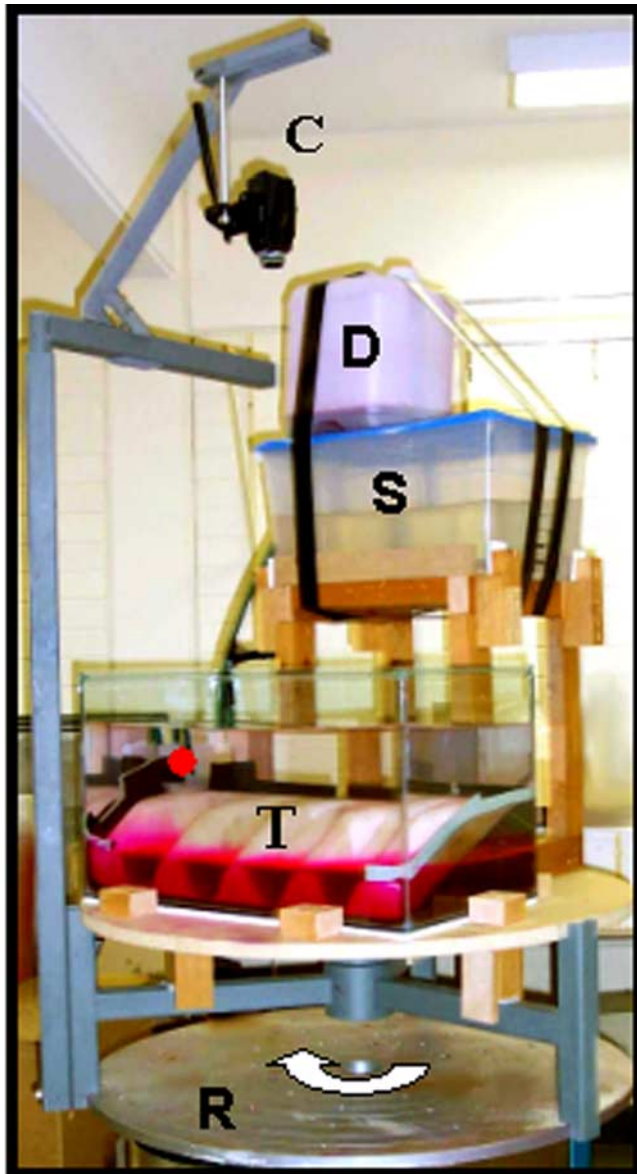
Figure 3. Design of the rotation tank experiments. See text for further details.
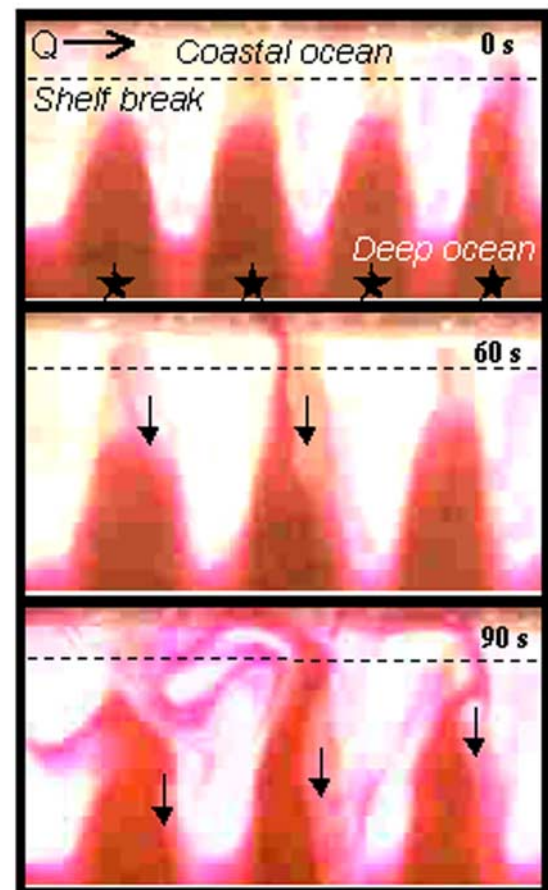

Figure 11. Laboratory experiment. Plane views showing spatial distributions of the interface of the bottom layer (red dye) (top) initially, (middle) after 60 s = 4.4 inertial periods, and (bottom) after 90 s = 6.7 inertial periods. Submarine channels run from top to bottom in each frame. Stars indicate locations of canyon axes. The source (Q) of dense shelf water is located in the upper left corner in each frame. Arrows highlight descending dense-water plumes.